PROTEIN DESIGN

De novo design of tunable, pH-driven conformational changes

Scott E. Boyken[1,2], Mark A. Benhaim[3], Florian Busch[4], Mengxuan Jia[4], Matthew J. Bick[1,2], Heejun Choi[5], Jason C. Klima[1,2], Zibo Chen[1,2,6], Carl Walkey[1,2], Alexander Mileant[3,6], Aniruddha Sahasrabuddhe[4], Kathy Y. Wei[1,2,7], Edgar A. Hodge[3], Sarah Byron[2], Alfredo Quijano-Rubio[1,2,8], Banumathi Sankaran[9], Neil P. King[1,2], Jennifer Lippincott-Schwartz[5], Vicki H. Wysocki[4], Kelly K. Lee[3,6], David Baker[1,2,10]*

The ability of naturally occurring proteins to change conformation in response to environmental changes is critical to biological function. Although there have been advances in the de novo design of stable proteins with a single, deep free-energy minimum, the design of conformational switches remains challenging. We present a general strategy to design pH-responsive protein conformational changes by precisely preorganizing histidine residues in buried hydrogen-bond networks. We design homotrimers and heterodimers that are stable above pH 6.5 but undergo cooperative, large-scale conformational changes when the pH is lowered and electrostatic and steric repulsion builds up as the network histidine residues become protonated. The transition pH and cooperativity can be controlled through the number of histidine-containing networks and the strength of the surrounding hydrophobic interactions. Upon disassembly, the designed proteins disrupt lipid membranes both in vitro and after being endocytosed in mammalian cells. Our results demonstrate that environmentally triggered conformational changes can now be programmed by de novo protein design.

De novo protein design is based on the principle that proteins fold to their lowest free-energy state (*1*): To design a new protein structure, an amino acid sequence is sought for which the intended structure is the lowest energy state encoded by that sequence. Advances in computational methods to search through the very large space of possible sequences and structures, together with improved energy functions, have made it possible to accurately design a wide variety of hyperstable proteins in very deep energy minima (*2*, *3*). Although such protein "rocks" can be useful for binding and scaffolding, much of biological function depends on proteins switching between alternative states driven by changes in environmental conditions. For example, the hemagglutinin (HA) protein on the surface of the influenza virus undergoes a large-scale, pH-dependent conformational change after uptake into the endosomes of target cells, which exposes a hydrophobic fusion peptide and drives membrane fusion (*4*–*6*). The encoding of such conformational switches in natural proteins can be quite complex to decipher and presents a challenge to de novo design because a sequence must be found that not only folds to the desired target structure, but also undergoes the desired conformational change in response to prespecified changes in solution conditions. Encoding such switching into a single amino acid sequence is likely to considerably compromise the stability of the original target structure.

Previous efforts to engineer proteins that respond to changes in pH have used either experimental selection for the desired pH response (*7*–*11*) or coiled coils containing histidine or glutamate residues (*12*–*17*), but the pH response in these systems can be difficult to predict and tune. We sought to create tunable, pH-responsive oligomers (pROs) by de novo design of parametric helical bundles with extensive histidine-containing networks spanning the subunit interfaces in which the histidine N_ϵ and N_δ atoms each make hydrogen bonds (Fig. 1). We reasoned that protonation of the histidine residues at low pH would disrupt the hydrogen-bond networks and result in both steric and electrostatic repulsion across the subunit interfaces (Fig. 1A). The repeating geometric cross sections of parametric helical bundles allow hydrogen-bond networks to be added or subtracted in a modular fashion, making it possible to tune the pH range of disassembly, as well as the cooperativity, by varying the number of histidine networks relative to the surrounding hydrophobic contacts.

We used a three-step procedure to computationally design helical bundles with extensive histidine-containing hydrogen-bond networks that span interhelical interfaces. First, large ensembles of oligomeric protein backbones with an inner and outer ring of α helices were produced by systematically varying the superhelical parameters in the Crick-generating equations (*18*, *19*). Each inner helix was connected to an outer helix through a short, designed loop to produce helix-turn-helix monomer subunits. Second, Rosetta HBNet (*20*) was extended to computationally design networks with buried histidine residues that accept a hydrogen bond across the oligomeric interface and then used to select the very small fraction of backbones that accommodate multiple histidine networks (see "Computational design methods" in the supplementary materials). Third, the sequence of the rest of the protein (surface residues and the hydrophobic contacts surrounding the networks) was optimized while keeping the histidine networks constrained using RosettaDesign (*21*, *22*) as described previously (*20*, *23*). Synthetic genes encoding five parent designs (homotrimers pRO-1 to pRO-3 and heterodimers pRO-4 and pRO-5) with multiple histidine-containing hydrogen-bond networks and complementary hydrophobic packing around the networks were constructed (table S1), and the proteins were expressed in *Escherichia coli*.

The designed proteins were well expressed, soluble, and readily purified by nickel-nitrilotriacetic acid (Ni-NTA) affinity chromatography, hexahistidine tag cleavage, and a second Ni-NTA step followed by gel filtration. Oligomeric state was assessed by size-exclusion chromatography (SEC) and native mass spectrometry (*24*). All parent designs assembled to the intended oligomeric state at pH 7 (Fig. 1) except for homotrimer design pRO-1, which appeared by SEC to be trimeric at high concentrations but was primarily dimeric by native mass spectrometry at lower concentrations (fig. S1); pRO-1 contains smaller disjoint networks, each with a single histidine, whereas the successful parent designs all have highly connected hydrogen-bond networks that span across all helices of the bundle cross section. To assess the effectiveness of the design strategy, we used native mass spectrometry to study the effect of pH on oligomerization state (*25*, *26*) from pH 7 down to pH 3 (see materials and methods in the supplementary materials); designs pRO-2 through pRO-5 all exhibited pH-induced loss of the initial oligomeric state (Fig. 1). Design pRO-2 was chosen for further characterization, as it exhibited pH-induced disassembly between pH 5 and 6, which is within the range of endosomal pH (*27*, *28*).

The pH-dependent conformational change is due to the designed histidine networks

To specifically evaluate the role of the histidine networks in the pH-induced transition of pRO-2, we sought to design a variant that lacked the histidine residues but was otherwise identical in sequence. Mutating all histidine residues to asparagine resulted in poor expression and aggregation, likely because the buried asparagine

[1]Department of Biochemistry, University of Washington, Seattle, WA 98195, USA. [2]Institute for Protein Design, University of Washington, Seattle, WA 98195, USA. [3]Department of Medicinal Chemistry, University of Washington, Seattle, WA 98195, USA. [4]Department of Chemistry and Biochemistry, The Ohio State University, Columbus, OH 43210, USA. [5]Howard Hughes Medical Institute, Janelia Research Campus, Ashburn, VA 20147, USA. [6]Graduate Program in Biological Physics, Structure, and Design, University of Washington, Seattle, WA, USA. [7]Department of Bioengineering, University of California, Berkeley, CA 94720, USA. [8]Department of Bioengineering, University of Washington, Seattle, WA 98195, USA. [9]Molecular Biophysics and Integrated Bioimaging, Lawrence Berkeley National Laboratory, Berkeley, CA, 94720. [10]Howard Hughes Medical Institute, University of Washington, Seattle, WA 98195, USA.
*Corresponding author. Email: dabaker@uw.edu

residues are unable to participate in hydrogen bonds; using HBNet, we rescued the histidine-to-asparagine mutations by generating networks in which all buried polar atoms participate in hydrogen bonds (Fig. 1B, blue cross sections). This new design (pRO-2-noHis), which differs by only six amino acids in each subunit, was well behaved in solution and assembled to the intended trimeric state, but unlike pRO-2, remained trimeric at low pH (Fig. 1C and fig. S3). Circular dichroism (CD) experiments showed that both proteins were helical and well folded, and chemical denaturation by guanidinium chloride (GdmCl) showed that pRO-2 had decreased folding stability at low pH, whereas pRO-2-noHis stability was unaffected by the change in pH (Fig. 1D). The histidine residues of pRO-2 do not participate in unintended metal interactions that contribute to assembly or disassembly, as addition of 10 mM EDTA had no effect on the helical fold or thermostability of design pRO-2 (fig. S2). Collectively, these results indicate that the observed pH response is due to the designed histidine networks.

To test the modularity of our design strategy, as well as to generate additional constructs for crystallization, we made designs that combined networks from pRO-2 and pRO-2-noHis (table S1). These variants remained soluble after disassembly at low pH and reassembled to their designed oligomeric state when the pH was raised

back to 7 (fig. S4). Unlike pRO-2 and pRO-2-noHis, designs pRO-2.3 and pRO-2.5 readily crystallized and x-ray crystal structures were determined at 1.28- and 1.55-Å resolution, respectively (Fig. 2, fig. S5, and table S2). Design pRO-2.3 (Fig. 2A), which differs from parent design pRO-2 by only two amino acids in each subunit, contains two histidine networks (red cross sections) and one nonhistidine polar network (blue cross section); the remaining layers (black cross section) are hydrophobic. Design pRO-2.5 differs from pRO-2 by five amino acids in each subunit and contains one histidine network and two nonhistidine networks. In all cases, the hydrogen-bond networks were nearly identical between the experimentally determined structures and the design models (Fig. 2). The ability to interchange hydrogen-bond networks at each layer without sacrificing structural accuracy highlights the modularity of our design strategy.

Tuning of pH set point and cooperativity

To take advantage of this modularity to systematically tune the pH response, we generated additional designs based on pRO-2 with different numbers of pH-independent hydrophobic layers (n), pH-dependent hydrogen-bond network layers each containing three histidine residues (m), and hydrogen-bond network layers lacking histidine (l), by swapping one or two of the histidine

networks (Fig. 3A, red cross sections) for either hydrophobic-only interactions (Fig. 3A, black cross sections) or the equivalent hydrogen-bond network lacking histidine (Fig. 3A, blue cross sections) in different combinations. To guide understanding of how the transition pH and cooperativity depend on the numbers of each type of layer, we developed a simple model of the pH dependence of the free energy of assembly as a function of n, m, and l (supplementary materials; eqs. S1 and S2) that assumes for simplicity that the protonation of individual histidine residues within a network layer is cooperative; this is plausible because the protonation of one histidine residue will likely disrupt the surrounding network, making the remaining histidine residues more accessible and raising their pK_a's by substantially reducing the free-energy cost of protonation (further discussion of the validity of this assumption is provided in the supplementary materials). Estimates of the contribution of each layer type to the overall free energy of assembly were obtained from guanidine denaturation experiments (Fig. 3B and fig. S6; supplementary materials). Model calculations using these values (Fig. 3C) show that increases in n shift the pH of disassembly to lower pH values without substantially affecting cooperativity (Fig. 3C, top), and varying m while n and ($m + l$) are kept constant changes the steepness of
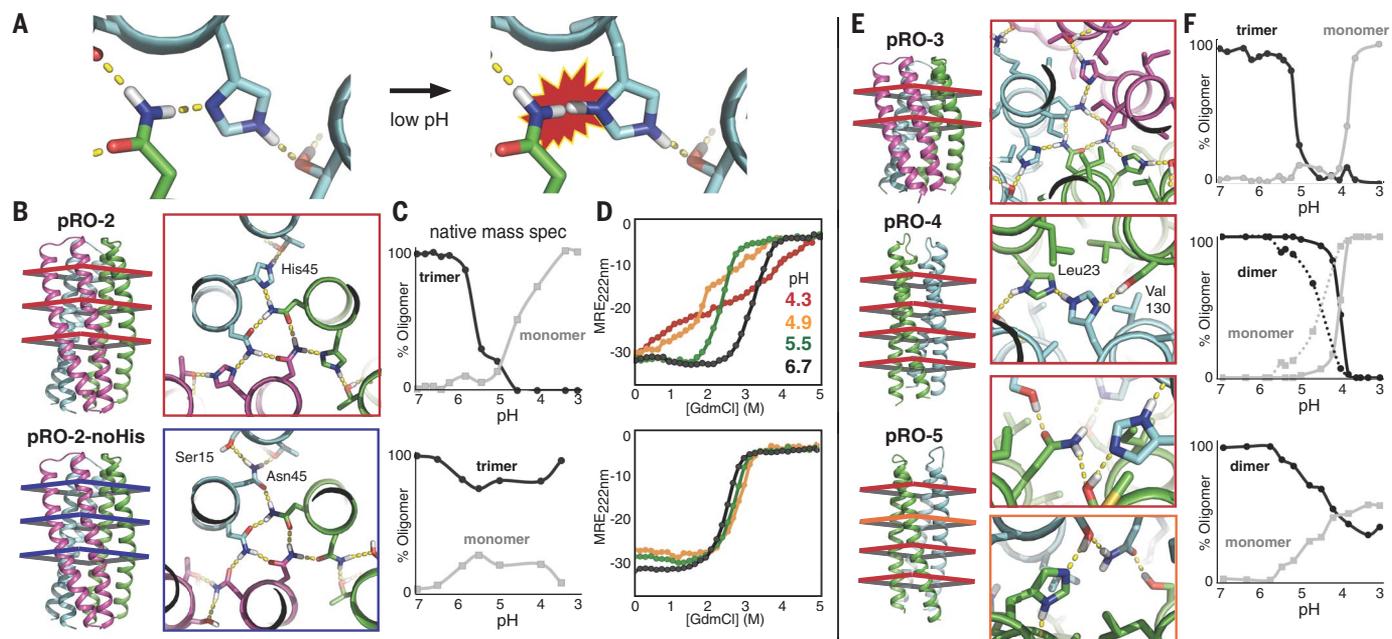
Fig. 1. Design of pROs. Design models are colored by subunit (green, cyan, and magenta), and red boxes indicate cross sections that contain the histidine hydrogen-bond networks. (**A**) Design strategy: Preorganized histidine residues destabilize intermolecular interfaces upon protonation at low pH. (**B**) The histidine-containing hydrogen-bond networks of design pRO-2 (red box, top) are replaced in pRO-2-noHis with networks containing no histidines, but with all buried polar atoms satisfied by hydrogen bonds (blue box, bottom). (**C**) pRO-2 (top), but not pRO-2-noHis (bottom), undergoes cooperative, pH-dependent quaternary structure dissociation when the pH is decreased below 5.5. Native mass spectrometry was performed at the indicated pH values at 5 μM trimer. (**D**) The stability of pRO-2 (top), but not pRO-2-noHis

(bottom), is strongly pH dependent, as indicated by chemical denaturation with GdmCl monitored by CD mean residue ellipticity (MRE) at 222 nm. (**E**) Designed histidine-containing homotrimer pRO-3 and heterodimers pRO-4 and pRO-5. (**F**) pH-induced disassembly of designs in (F) monitored by native mass spectrometry; L23A/V130A mutations designed to weaken the interface of pRO-4 increase pH sensitivity (dashed lines) compared with the parent design (solid lines). In (C) and (F), % oligomer is plotted as the percentage of that species relative to all oligomeric species observed at each pH value; for clarity, not all species are shown, and in several cases, other oligomeric species were observed at intermediate pH values during the transition to monomer (fig. S14).
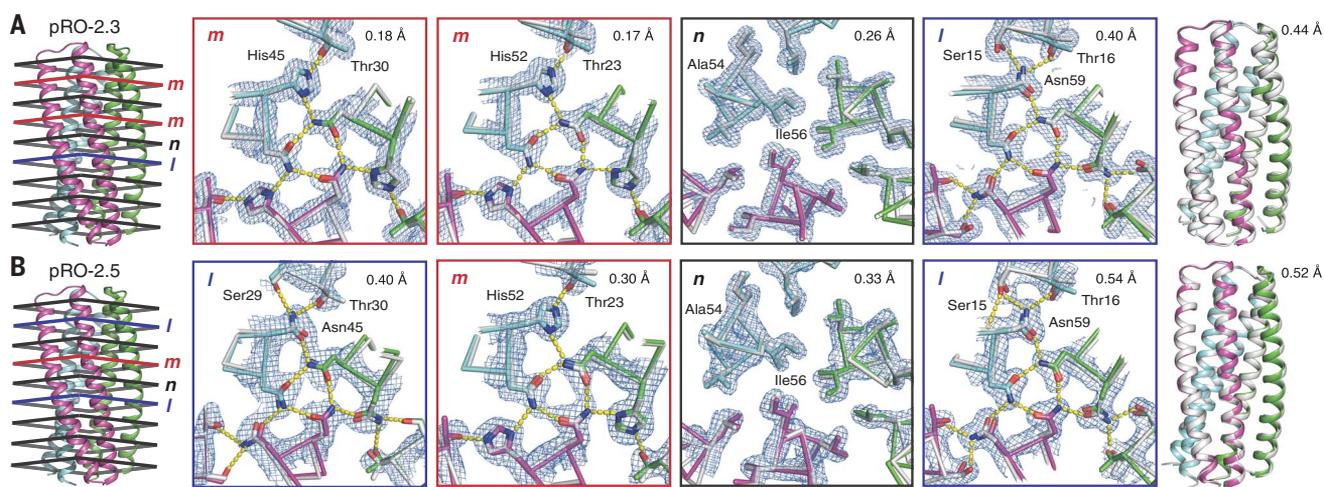
Fig. 2. High-resolution x-ray crystal structures are very close to design models. Left, design model schematic; middle, comparison of selected cross sections to crystal structure; right, backbone superposition to crystal structure. (**A** and **B**) Design pRO-2.3 (A) and design pRO-2.5 (B): Design models (colored by subunit) of pRO-2.3 and pRO-2.5 are in close agreement with x-ray crystal structures (white): electron density (blue mesh) is shown at a level of 1.0 Å; root mean square deviation values between crystal structure and design model are given for heavy-atom superposition of the side chains shown in the boxes, and for all backbone atoms (right). Cross sections in boxes are labeled as in the theoretical model (supplementary materials, eqs. S1 and S2): hydrophobic layers (n, black), histidine network layers (m, red), and polar network layers lacking histidine (l, blue). Protein Data Bank (PDB) accession codes are 6MSQ (pRO-2.3) and 6MSR (pRO-2.5).
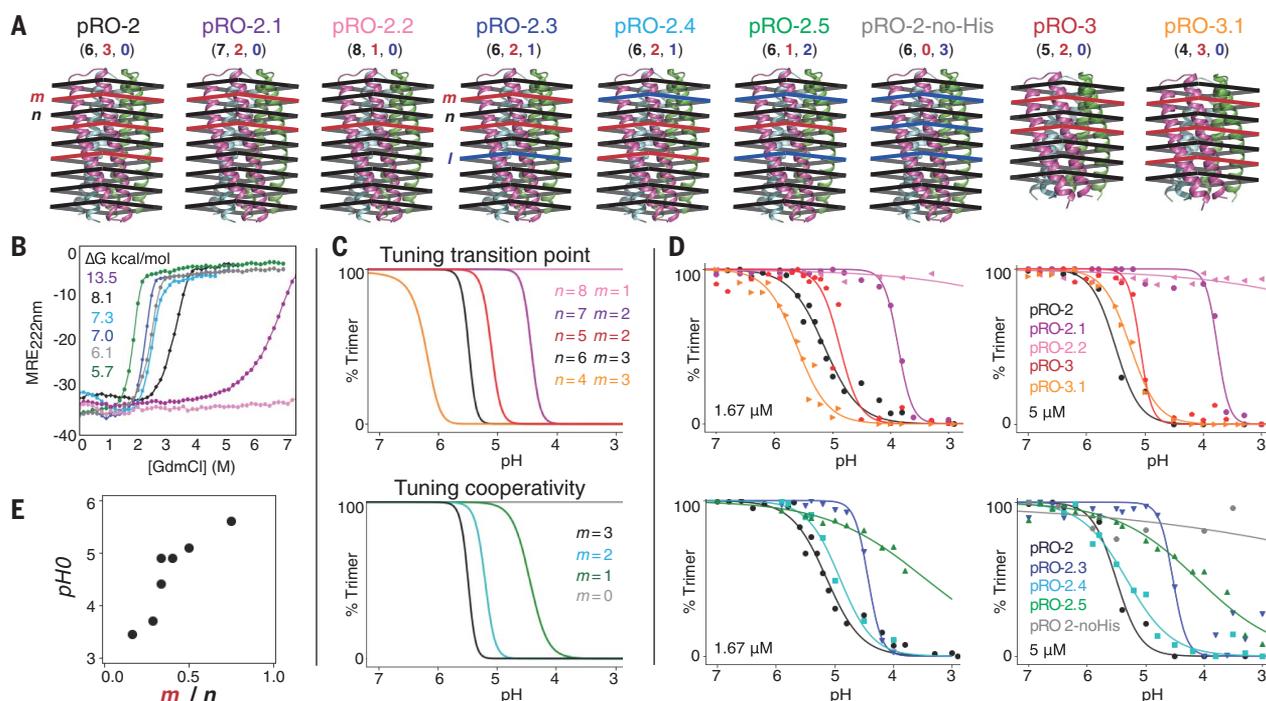
Fig. 3. Systematic tuning of pH transition point and cooperativity. (**A**) Schematics of designs with different combinations of hydrophobic layers (n, black), histidine network layers (m, red), and polar network layers lacking histidine (l, blue); the number of each layer type is given in parentheses as (n, m, l). (**B**) Chemical denaturation by GdmCl at pH 7.4 measured by CD MRE monitoring helicity at 222 nm; curves are colored according to their design names in (A) with estimates of unfolding free energies (fig. S6) displayed in the inset. (**C**) Theoretical model: pH dependence of trimer abundance according to eq. S2; each curve corresponds to the values of m, n, and l for a design in (A) and they are colored accordingly. Curves were generated using parameter values $\Delta G_{hydrophobic}$ = 2.7 kcal/mol, ΔG_{polar_m} = −2.8 kcal/mol, and ΔG_{polar_l} = −3.41 kcal/mol, estimated from chemical denaturation experiments (B) (fig. S6, supplementary materials). (**D**) Native mass spectrometry–monitored, pH-induced quaternary structure disruption of the designs in (A) at 1.67 or 5 μM with respect to the trimeric species; curves were fit to the experimental data using eq. S3. (**E**) The higher the ratio of m to n (x axis), the higher the pH transition point pH_0 (y axis).

the transition (Fig. 3C, bottom). Qualitatively, the pH set point—the pH at which the free energy of disassembly is zero—is determined by the balance between the overall intrinsic stability of the protein at neutral pH (which increases with n) and the magnitude of the pH-dependent destabilization (which increases with m), whereas the transition cooperativity is determined by the total number of protonatable histidine residues (which increases with m). The designs of Fig. 3A were assessed by native mass spectrometry and found to assemble to the intended trimeric state at pH 7 and to disassemble at a range of pH values (Fig. 3D) that are qualitatively in agreement with the model calculations described previously.

The larger the number of hydrophobic layers (n), the greater the predicted stability and hence the lower the predicted transition pH (Fig. 3C). Indeed, replacing a single histidine network with a hydrophobic network (design pRO-2.1; Fig. 3D, top, purple curves) shifts the transition pH from above 5 down to ~3.5, and replacing two histidine networks with hydrophobic networks (design pRO-2.2; Fig. 3D, top, pink curves) eliminates the pH response altogether. Designs pRO-3 (Fig. 3D, top, red curves) and pRO-3.1 (Fig. 3D, top, orange curves) have two fewer total layers than pRO-2 and also behave as predicted: Replacing a single histidine network layer with a hydrophobic layer in these shorter designs increases the pH set point. Over the full set of designs tested, the larger the ratio of hydrophobic layers (n) to histidine layers (m), the higher the transition pH (Fig. 3E; see supplementary materials for discussion).

Decreasing the total number of histidine residues without substantially altering stability is predicted to decrease the cooperativity (steepness) of the transition (Fig. 3C, bottom). Indeed, replacing the histidine networks (m) with polar networks lacking histidine residues (l) that have roughly equal contribution to stability at neutral pH allows for tuning of the cooperativity of disassembly (Fig. 3D, bottom) with little effect on stability (Fig. 3B). At 5 μM trimer (Fig. 3D, bottom right), the transition cooperativity decreases

through the series ($m = 3$, $l = 0$) (black) through ($m = 2$, $l = 1$) (cyan) to ($m = 1$, $l = 2$) (green), consistent with this expectation and the simple model. Indeed, design pRO-2.5 (green curves), which has only one histidine network, is the least cooperative design tested and disassembles at ~pH 4 (Fig. 3D, bottom), despite having the lowest stability in chemical denaturation experiments (Fig. 3B). Overall, the model is in qualitative agreement with experimental observations; the designs have predicted transition pH values that are within ~0.5 pH units of experimentally observed values (table S3 and fig. S7).

Context dependence

Although the simple model qualitatively accounts for the dependence of disassembly and cooperativity on m, n, and l, the location of the histidine network layers also contributes. For example, pRO-2.3 and pRO-2.4 have identical layer compositions (Fig. 3A) and nearly identical sequence compositions (table S1), but pRO-2.4 disassembles at a higher transition pH and is less cooperative (Fig. 3D). Overall, designs with a histidine network close to the termini (e.g., pRO-2.4) have higher transition pH values and less cooperative transitions (fig. S7). Designs pRO-2.1 and pRO-2.3, which do not have histidine networks close to their termini, have predicted measurements of cooperativity that are close to experimentally observed values (table S3). Our simple model assumes that the histidine residues have sufficiently low pK_a values in the folded state that protonation only occurs upon disassembly, but that histidine residues close to the termini could have a higher pK_a if exposed in local conformational fluctuations of the termini, allowing some accommodation of protonation in the trimeric state. Consistent with this hypothesis, designs pRO-2 and pRO-2.4, which have histidine networks closer to the termini, have higher flexibility as assessed by small-angle x-ray scattering (SAXS) measurements (29, 30) compared with designs pRO-2.1, pRO-2.3, pRO-2.5, and pRO-2-noHis, which do not have histidine networks close to the termini (fig. S8 and table S4);
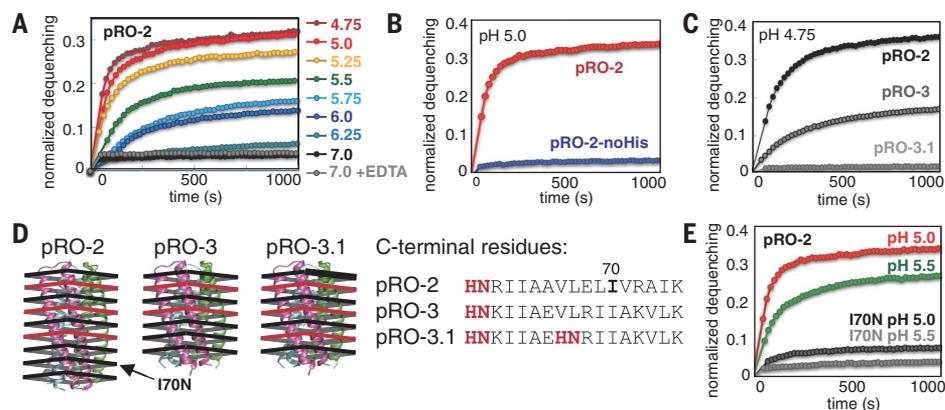
a correlation between flexibility and reduced cooperativity is also observed when the ordered helix-connecting loops are replaced by a flexible Gly-Ser (GS) linker (fig. S9). Designs with histidine networks farther away from the termini (and closer to the loop in the helical hairpin subunit) are presumably harder to initially protonate (with very low pK_a's), but once protonated, the histidine residues have a greater destabilizing effect that increases the accessibility of the other histidine positions, resulting in a more cooperative transition.

pH-dependent membrane disruption

The trimer interface contains a number of hydrophobic residues that become exposed upon pH-induced disassembly; because amphipathic helices can disrupt membranes (17, 31), we investigated whether the designed proteins exhibit pH-dependent interactions with membranes. Purified protein with the hexahistidine tag removed was added to synthetic liposomes containing the pH-insensitive fluorescent dye sulforhodamine B (SRB) at self-quenching concentrations over a range of pH values; leakage of liposome contents after disruption of the lipid membrane can be monitored through dequenching of the dye (32). Design pRO-2 caused pH-dependent liposome disruption at pH values as high as 6, with maximal activity around pH 5 (Fig. 4A); disruption was observed over a range of lipid compositions (fig. S10). Design pRO-2-noHis, which did not disassemble at low pH (Fig. 1, C and D), showed no liposome activity at pH 5 (Fig. 4B). Design pRO-3, but not pRO-3.1 (which is even more pH sensitive than design pRO-3; Fig. 3D), also caused pH-dependent liposome disruption (Fig. 4C). Unlike pRO-3 and pRO-2, pRO-3.1 lacks a contiguous stretch of hydrophobic amino acids at the C terminus (Fig. 4D); to test the importance of this feature, we mutated a central isoleucine in this region of pRO-2 to asparagine (I70N), which resulted in attenuation of pH-induced liposome disruption (Fig. 4E). Our designs mirror the behavior of naturally occurring membrane fusion proteins, such as influenza

Fig. 4. pH-dependent membrane disruption. Proteins were added to synthetic liposomes encapsulating quenched SRB fluorescent dye; activity is measured by normalized dequenching of dye that leaks out from disrupted membranes. (**A**) Design pRO-2 disrupts liposomes in a pH-dependent manner; colors correspond to different pH values (shown on right). (**B**) pRO-2-noHis, which is not pH responsive (Fig. 1, C and D), does not disrupt liposomes at pH 5. (**C**) Design pRO-3 shows liposome disruption activity at pH 4.75, whereas pRO-3.1 does not, despite pRO-3.1 being more pH responsive (Fig. 3D). (**D**) Comparison of pRO-2, pRO-3, and pRO-3.1 suggests that the membrane-interacting region is the contiguous hydrophobic stretch at the C terminus (right):

in pRO-3.1, additional histidine network residues (red) interrupt the contiguous hydrophobic stretch. Single-letter abbreviations for the amino acid residues are as follows: A, Ala; E, Glu; F, Phe; H, His; I, Ile; K, Lys; L, Leu; N, Asn; R, Arg; V, Val; and W, Trp. (**E**) pRO-2 I70N mutation attenuates liposome activity. Final protein concentration is 2.5 μM with respect to monomer. Data compared within each single plot were collected using the same batch of liposomes.

C-terminal residues:
pRO-2 **HN**RIIAAVLEL**I**VRAIK
pRO-3 **HN**KIIAEVLRIIAKVLK
pRO-3.1 **HN**KIIAE**HN**RIIAKVLK

HA, in undergoing conformational rearrangements that expose the hydrophobic faces of amphipathic α helices, allowing them to interact with membranes (*4–6*).

To increase the pH of disassembly closer to that of early endosomes (~5.5 to 6), we decreased the overall interface affinity through mutations in the hydrophobic layers (tuning $\Delta G_{hydrophobic}$ in eq. S2) of design pRO-2. Consistent with the model (supplementary materials, eq. S2), increasing $\Delta G_{hydrophobic}$ through the A54M substitution decreases the transition pH, whereas weakening $\Delta G_{hydrophobic}$ with the I56V substitution increases the transition pH to ~5.8 (Fig. 5A). Neither of the mutations substantially affect the cooperativity of the transition (Fig. 5B and table S3).

CD-monitored denaturation experiments showed that A54M increases stability and I56V decreases stability, as expected (fig. S11). Similar tuning of the heterodimer design pRO-4 with the destabilizing mutations L23A/V130A increased the disassembly transition pH from 4 to 5. (Fig. 1F).

To characterize the physical interactions between protein and membranes and the mechanism of membrane disruption, purified proteins were chemically conjugated to gold nanoparticles and visualized by cryo–electron microscopy and tomography. Design pRO-2 I56V, which has a higher transition pH (Fig. 5A), also has increased liposome permeabilization activity (Fig. 5B); it directly interacts with liposomes at pH 5 but not at pH 8, whereas the non–pH-responsive

design pRO-2-noHis shows no interactions with liposomes at either pH (Fig. 5C and fig. S12). We observed widespread membrane deformation and disruption of the lipid bilayer with design pRO-2 I56V and pRO-2 at pH 5, along with association of protein-conjugated gold nanoparticles to liposomes (Fig. 5C and fig. S12). At either pH for pRO-2-noHis, and at pH 8 for pRO-2 I56V, there were no signs of membrane deformation or disruption, and protein-conjugated gold nanoparticles were well dispersed and did not associate to the membrane (Fig. 5, C and D, and fig. S12). At pH 5, design pRO-2 I56V caused substantial deformation of the liposomal membrane and induced the formation of tight extended interfaces between liposomes; density at
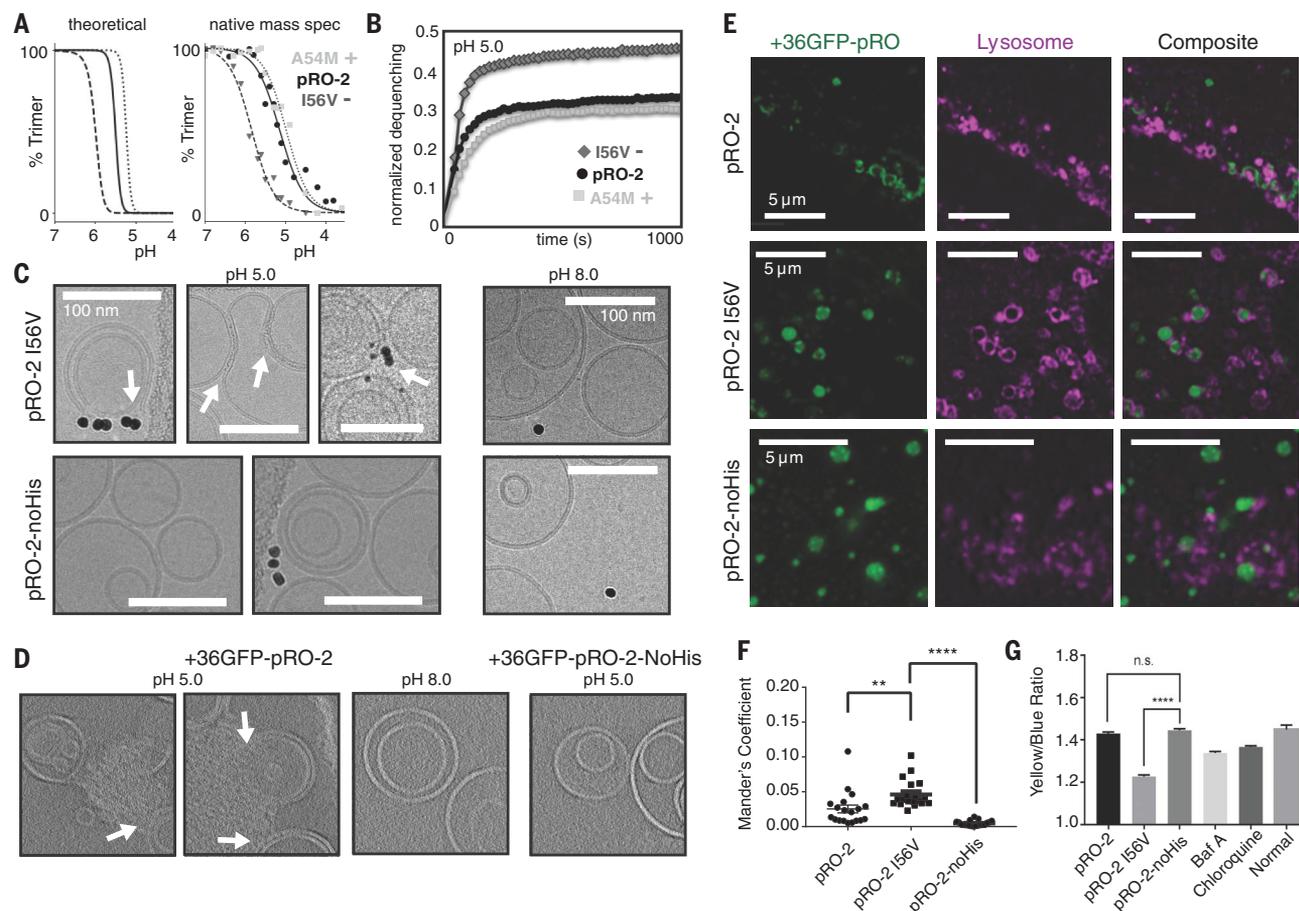
Fig. 5. Imaging of pH-induced membrane permeabilization. (**A**) Tuning $\Delta G_{hydrophobic}$ by mutagenesis to alter the pH sensitivity of pRO-2; (left) theoretical curves (from eq. S2) for pRO-2, I56V, and A54M; (right) native mass spectrometry of pRO-2 compared with I56V and A54M mutants. The transition pH is shifted as predicted without substantially affecting cooperativity; data are fit to eq. S3 as in Fig. 3. (**B**) pRO-2 I56V has increased membrane permeabilization activity (assay as in Fig. 4). (**C**) Cryo–electron microscopy using purified proteins conjugated to gold nanoparticles: design pRO-2 I56V interacts directly with liposomes at pH 5, but not at pH 8, whereas pRO-2-noHis does not interact with liposomes at either pH. At low pH, design pRO-2 I56V deforms liposomes and induces the formation of tight extended interfaces between liposomes (white arrow in top middle panel; density between membranes is likely pRO-2 I56V). In all control conditions, liposomes were unperturbed and free

protein–conjugated gold nanoparticles were well dispersed. Scale bars, 100 nm. (**D**) Electron tomography of +36 GFP fusions to pRO-2 and pRO-2-noHis at pH 5 or 8. (**E**) Fluorescence imaging of +36 GFP fusions to designs pRO-2, pRO-2 I56V, and pRO-2-noHis and composite correlation with lysosome membrane staining in U2-OS cells. pRO-2 I56V, but not pRO-2-noHis, is clearly localized within lysosomes; the pRO-2-noHis staining is likely from protease-resistant aggregates. (**F**) Mander's colocalization coefficients representing the fraction +36 GFP fusion proteins that colocalize with lysosomal membrane. (**G**) Ratios of yellow emission and blue emission on U2-OS loaded with LysoSensor Yellow–Blue DND-160 after 1 hour of incubation of pRO-2 (5 μM), pRO-2 I56V (5 μM), pRO-2-noHis (5 μM), bafilomycin A (Baf A; 1 μM), chloroquine (50 μM), and medium (normal). The lower the ratio, the higher the lysosome pH; pRO-2 I56V increases the lysosomal pH more than the small-molecule drugs do.

these interfaces likely corresponds to the designed protein (Fig. 5C and fig. S12).

In the low-pH environment of the mammalian cell endocytic pathway, internalized proteins are either recycled back to the cell surface or destined for degradation by fusion with lysosomes, where the lower pH activates hydrolytic enzymes (33). To test their behavior in the endocytic pathway, we expressed the pRO-2 trimers as fusions to +36 GFP (green fluorescent protein) (34, 35) to facilitate both fluorescent imaging and endocytosis. After incubation with U2-OS cells, purified GFP fusions of pRO-2 and I56V are internalized and colocalize with lysosomal membranes, whereas a GFP fusion to pRO-2-noHis is not colocalized (Fig. 5, E and F). I56V, which is the most pH-sensitive and membrane-active design in this study (Fig. 5, A to C), is the most strongly colocalized with the lysosomal membrane (Fig. 5F). We hypothesize that all three proteins are endocytosed and traffic to the lysosome, but once there, pRO-2-noHis is degraded whereas pRO-2 and I56V remain intact because, after disassembly in the low-pH environment of the endosome and lysosome, the latter two proteins insert into membranes, cause proton leakage, and increase the lysosomal pH, reducing activation of lysosomal proteases. To test this hypothesis, we incubated U2-OS cells loaded with dye to track pH (LysoSensor Yellow–Blue DND-160) for 1 hour with pRO-2 (5 μM), pRO-2 I56V (5 μM), or pRO-2-noHis (5 μM); pRO-2 I56V was found to raise the lysosomal pH compared with pRO-2-noHis and untreated cell controls (Fig. 5G and fig. S12). Design pRO-2 produced larger changes in lysosomal pH than bafilomycin A and chloroquine, two drugs known to neutralize lysosomal pH (Fig. 5G).

Conclusions

Cooperativity and allostery are hallmarks of the regulation of protein activity. The Monod-Wyman-Changeux model (36), proposed more than 50 years ago, explained the high cooperativity that allows proteins to substantially alter function in response to small changes in the environment by postulating that in a homo-oligomeric conformational transition, the monomers in the dominant populated states all have the same conformation (i.e., there are no mixed conformer states). It has not been clear how much evolutionary fine-tuning was required to achieve this high cooperativity and the resulting environmental sensitivity, and whether such high cooperativity could be achieved in a completely de novo–designed system. We show that high cooperativity can indeed be achieved in a designed system: The loss of trimer pRO-2 over a very narrow pH range (Fig. 3D) is as cooperative as pH-induced conformational changes in natural protein systems. Because of the modularity of the design concept, and in contrast to naturally oc-

curring pH switches, the set point and cooperativity of the conformational change can be systematically tuned.

The liposome-permeabilizing activity of the designs makes them attractive starting points for approaching the challenge of delivery of biologics into the cytoplasm through endosomal escape. Delivery methods relying on cell-penetrating peptides, supercharged proteins, and lipid-fusing chemical reagents can be toxic because of nonspecific interactions with many types of membranes in a pH-independent manner (34, 37, 38). Viral vectors achieve intracellular delivery through membrane-active proteins, many of which are activated by the lower-pH environment of the endosome, but can be complicated by preexisting immunity and difficulties in reprogramming. A designed protein-only system capable of pH-induced endosomal escape could rival the delivery efficiency of viruses without the inherent disadvantages.

REFERENCES AND NOTES

1. C. B. Anfinsen, *Science* **181**, 223–230 (1973).
2. P.-S. Huang, S. E. Boyken, D. Baker, *Nature* **537**, 320–327 (2016).
3. G. J. Rocklin et al., *Science* **357**, 168–175 (2017).
4. C. M. Carr, P. S. Kim, *Cell* **73**, 823–832 (1993).
5. J. M. White, S. E. Delos, M. Brecher, K. Schornberg, *Crit. Rev. Biochem. Mol. Biol.* **43**, 189–219 (2008).
6. C. M. Mair, K. Ludwig, A. Herrmann, C. Sieben, *Biochim. Biophys. Acta* **1838**, 1153–1168 (2014).
7. M. L. Murtaugh, S. W. Fanning, T. M. Sharma, A. M. Terry, J. R. Horn, *Protein Sci.* **20**, 1619–1631 (2011).
8. E.-M. Strauch, S. J. Fleishman, D. Baker, *Proc. Natl. Acad. Sci. U.S.A.* **111**, 675–680 (2014).
9. N. Gera, A. B. Hill, D. P. White, R. G. Carbonell, B. M. Rao, *PLOS ONE* **7**, e48928 (2012).
10. M. Dalmau, S. Lim, S.-W. Wang, *Biomacromolecules* **10**, 3199–3206 (2009).
11. T. Igawa et al., *Nat. Biotechnol.* **28**, 1203–1207 (2010).
12. K. Wada, T. Mizuno, J. Oku, T. Tanaka, *Protein Pept. Lett.* **10**, 27–33 (2003).
13. R. Lizatović et al., *Structure* **24**, 946–955 (2016).
14. K. Pagel et al., *J. Am. Chem. Soc.* **128**, 2196–2197 (2006).
15. C. Minelli, J. X. Liew, M. Muthu, H. Andresen, *Soft Matter* **9**, 5119–5124 (2013).
16. J. Aupič, F. Lapenta, R. Jerala, *ChemBioChem* **19**, 2453–2457 (2018).
17. Y. Zhang et al., *ACS Chem. Biol.* **10**, 1082–1093 (2015).
18. F. H. C. Crick, *Acta Crystallogr.* **6**, 685–689 (1953).
19. W. Grigoryan, W. F. Degrado, *J. Mol. Biol.* **405**, 1079–1100 (2011).
20. S. E. Boyken et al., *Science* **352**, 680–687 (2016).
21. B. Kuhlman, D. Baker, *Proc. Natl. Acad. Sci. U.S.A.* **97**, 10383–10388 (2000).
22. A. Leaver-Fay et al., in *Methods in Enzymology*, M. L. Johnson, L. Brand, Eds. (Academic Press, 2011), vol. 487, pp. 545–574.
23. P.-S. Huang et al., *Science* **346**, 481–485 (2014).
24. S. Mehmood, T. M. Allison, C. V. Robinson, *Annu. Rev. Phys. Chem.* **66**, 453–474 (2015).
25. E. Boeri Erba, K. Barylyuk, Y. Yang, R. Zenobi, *Anal. Chem.* **83**, 9251–9259 (2011).
26. N. Leloup et al., *Nat. Commun.* **8**, 1708 (2017).
27. Y.-B. Hu, E. B. Dammer, R.-J. Ren, G. Wang, *Transl. Neurodegener.* **4**, 18 (2015).
28. M. Grabe, G. Oster, *J. Gen. Physiol.* **117**, 329–344 (2001).
29. K. N. Dyer et al., *Methods Mol. Biol.* **1091**, 245–258 (2014).
30. S. Classen et al., *J. Appl. Crystallogr.* **46**, 1–13 (2013).
31. E. Eiríksdóttir, K. Konate, U. Langel, G. Divita, S. Deshayes, *Biochim. Biophys. Acta* **1798**, 1119–1128 (2010).
32. L. Gui, K. K. Lee, in *Influenza Virus: Methods and Protocols*, Y. Yamauchi, Ed. (Springer New York, New York, NY, 2018), pp. 261–279.
33. C. S. Pillay, E. Elliott, C. Dennison, *Biochem. J.* **363**, 417–429 (2002).
34. M. Li et al., *J. Am. Chem. Soc.* **137**, 14084–14093 (2015).
35. M. S. Lawrence, K. J. Phillips, D. R. Liu, *J. Am. Chem. Soc.* **129**, 10110–10112 (2007).
36. J. Monod, J. Wyman, J.-P. Changeux, in *Selected Papers in Molecular Biology by Jacques Monod*, A. Lwoff, A. Ullmann, Eds. (Academic Press, 1978), pp. 593–623.
37. E. L. Snyder, S. F. Dowdy, *Pharm. Res.* **21**, 389–393 (2004).
38. Y. S. Choi, M. Y. Lee, A. E. David, Y. S. Park, *Mol. Cell. Toxicol.* **10**, 1–8 (2014).

SUPPLEMENTARY MATERIALS

science.sciencemag.org/content/364/6441/658/suppl/DC1
Materials and Methods
Supplementary Text
Figs. S1 to S15
Tables S1 to S6
References (39–61)